

Decoupling the Voltage Hysteresis of Li-Rich Cathodes: Electrochemical Monitoring, Modulation Anionic Redox Chemistry and Theoretical Verifying

Gang Sun, Fu-Da Yu, Changtai Zhao, Ruizhi Yu, Samuel Farnum, Guangjie Shao,*
Xueliang Sun,* and Zhen-Bo Wang*

Cathodes in lithium-ion batteries with anionic redox can deliver extraordinarily high specific capacities but also present many issues such as oxygen release, voltage hysteresis, and sluggish kinetics. Identifying problems and developing solutions for these materials are vital for creating high-energy lithium-ion batteries. Herein, the electrochemical and structural monitoring is conducted on lithium-rich cathodes to directly probe the formation processes of larger voltage hysteresis. These results indicate that the charge-compensation properties, structural evolution, and transition metal (TM) ions migration vary from oxidation to reduction process. This leads to huge differences in charge and discharge voltage profile. Meanwhile, the anionic redox processes display a slow kinetics process with large hysteresis (≈ 0.5 V), compared to fast cationic redox processes without any hysteresis. More importantly, a simple yet effective strategy has been proposed where fine-modulating local oxygen environment by the lithium/oxygen (Li/O) ratio tunes the anionic redox chemistry. This effectively improves its electrochemical properties, including the operating voltage and kinetics. This is also verified by theoretical calculations that adjusting anionic redox chemistry by the Li/O ratio shifts the TM 3d—O 2p bands and the non-bonding O 2p band to a lower energy level, resulting in a higher redox reaction potential.

1. Introduction

Over the past three decades, researches concerning lithium-ion batteries (Li-ion batteries, LIBs) have grown tremendously and have been applied to every aspect of life, ranging from a variety of electronic productions to electric vehicles and smart grids. Nowadays, research related to LIBs is focusing on how to improve its energy density, safety, lifetime, and reduce its cost to satisfy the growing demands.^[1] Among the different research fields, the development of advanced cathodes is a key factor. Limited by their low capacities (< 200 mAh g⁻¹), traditional cathodes, such as layered oxides (LiNi_xCo_yMn_zO₂, $x + y + z = 1$, NCM), spinel oxides (LiMn₂O₄), and olivine phosphates (LiFePO₄), cannot meet the requirements for developing high-energy-density LIBs.^[2] The relatively low capacity of these materials is usually ascribed to the single cationic redox process. Recently, Li-rich cathodes (LR-NCMs) with both redox processes of cations and anions were proposed and attracted researchers' attention. These cathodes can deliver higher capacities up to 300 mAh g⁻¹ due to the process of multiple electrons transfer.^[3]


LR-NCMs, marked as $x\text{Li}_2\text{MnO}_3 \cdot (1-x)\text{LiTMO}_2$ (TM = Ni, Mn, and Co), are generally considered to be an aggregate of two phases: a layered monoclinic Li₂MnO₃ phase (C2/m space group) and a layered hexagonal LiTMO₂ phase (R-3m space group).^[4] Recently, researchers have put their attention on oxygen center chemistry to probe the redox processes in the cathode material (no matter for cationic redox, or anionic redox).^[5] In LiTMO₂ local coordination structure phase, only one type of O 2p orbital (the O 2p orbitals along with the Li-O-TM configurations) can be observed. This is similar to the conventional layered-oxide cathodes, tending to trigger cationic redox. While in Li₂MnO₃ local coordination structure phase, there are two types of O 2p orbital (the O 2p orbitals along with the Li-O-TM configurations and the Li-O-Li configurations, inset of Figure 1a). Meanwhile, the pure non-bonding O 2p states with high energy will be generated due to the existence of Li-O-Li configurations. Then, oxygen redox is mainly caused by these pure non-bonding O 2p states, rather than the σ bonding

Dr. G. Sun, Prof. G. Shao
State Key Laboratory of Metastable Materials Science and Technology
Hebei Key Laboratory of Heavy metal deep-remediation in water and resource reuse

College of Environmental and Chemical Engineering
Yanshan University
Qinhuangdao 066004, China
E-mail: shaoguangjie@ysu.edu.cn

Dr. G. Sun, Dr. F.-D. Yu, Prof. Z.-B. Wang
MIIT Key Laboratory of Critical Materials Technology
for New Energy Conversion and Storage
School of Chemistry and Chemical Engineering
State Key Lab of Urban Water Resource and Environment
Harbin Institute of Technology
Harbin 150001, China
E-mail: wangzhib@hit.edu.cn

Dr. G. Sun, Dr. C. Zhao, Dr. R. Yu, Dr. S. Farnum, Prof. X. Sun
Department of Mechanical and Materials Engineering
University of Western Ontario
Ontario N6A 5B9, Canada
E-mail: xsun9@uwo.ca

 The ORCID identification number(s) for the author(s) of this article can be found under <https://doi.org/10.1002/adfm.202002643>.

DOI: 10.1002/adfm.202002643

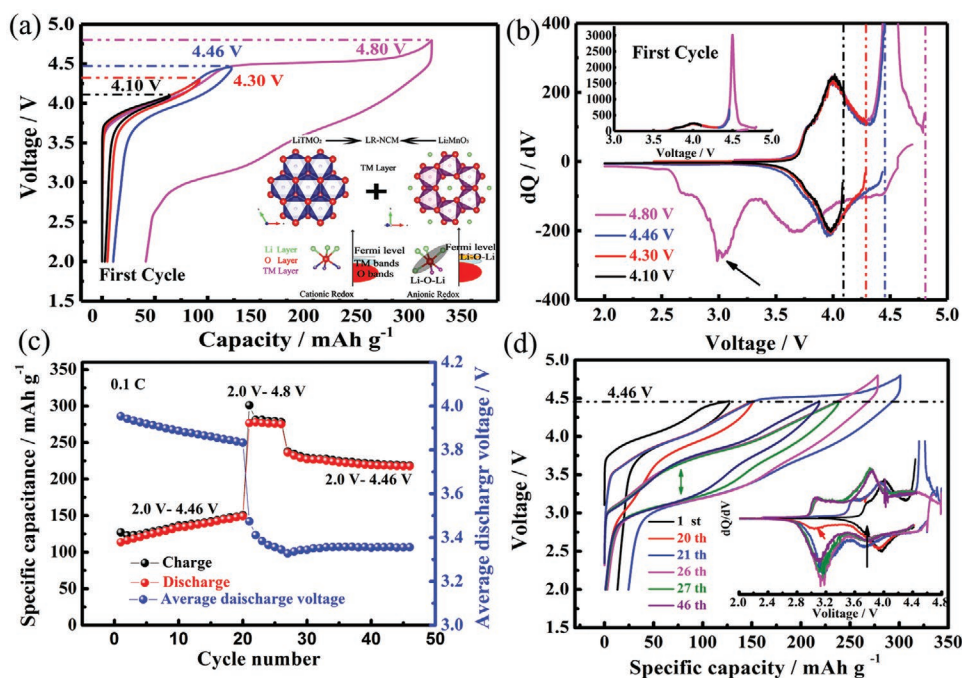


Figure 1. a) Charge/discharge curves of HL cell at pre-activation and activation cycles with consecutive upper cutoff voltages of 4.10, 4.30, 4.46, and 4.80 V, when cycled at 25 mA g^{-1} and room temperature ($25 \text{ }^\circ\text{C}$), the inset are the lattice of layered structures with a hexagonal LiTMO_2 phase and a monoclinic Li_2MnO_3 phase, and local coordination structure and schematic of the band structure of the two phases, different local coordination structures correspond to different redox mechanisms, the local coordination structure of LR-NCMs is generally considered to be an aggregate of two local coordination structures. b) The corresponding differential capacity (dQ/dV) plot of (a) data. c) Capacity and average discharge voltage versus cycle number for HL with a 2.0–4.46 V pre-activation cycle (1–20 cycles) and a 2.0–4.8 V activation cycle (21–25 cycles), and follow by a 2.0–4.46 V post-activation cycle (26–46 cycles) at 20 mA g^{-1} . d) Charge/discharge plots and dQ/dV for different cycles of HL.

states in the case of LiTMO_2 . Different local coordination structures correspond to different redox mechanisms, which may lead to significant differences in charge-discharge features.^[6]

However, recent studies declared that the redox of oxygen in LR-NCMs is a mixed blessing for the high-energy LIBs.^[7] On the one hand, the reversible redox of oxygen can provide a high capacity for LR-NCMs. On the other hand, researchers have linked some practical roadblocks of Li-rich cathodes (oxygen release, surface instability, voltage hysteresis, and sluggish kinetics) with anionic redox and the rearrangement/migration of transition metal (TM) ions. Doping anion/cation ions or surface modification of LR-NCMs have been proved effectively to improve its oxygen release or surface stability.^[8] But the fundamental insights about the relationship between voltage hysteresis and redox reaction of anions and cations are also indispensable for improving Li-rich cathodes. The main manifestation of voltage hysteresis is the differences in the charging/discharging path, and high capacity at a low voltage of about 3.1 V during discharge, which severely degraded the effective energy density. As for the high capacity at a low voltage ($\approx 3.1 \text{ V}$), a major debate lies in which redox reaction corresponded to this process. Shen et al.^[9] interpreted that the low-voltage dQ/dV peak ($\approx 3.1 \text{ V}$) is ascribed to the $\text{Mn}^{3+/4+}$ redox couple generated by the layered to spinel transformation of LR-NCMs during activation and cycling. However, William et al.^[7b] confirmed that partially reversible TM ion migration reorders the potentials of anionic and cationic redox during charging and discharging. TM ion migration also decreases the potential of the bulk

oxygen redox couple ($>1 \text{ V}$). Croy et al.^[7a] demonstrated that the voltage hysteresis in LR-NCMs is mainly due to an inherent structural rearrangement after an activation reaction of the Li_2MnO_3 phase that alters the crystallographic site energies via electrochemical measurements. Assat et al.^[10] indicated that the anionic redox exhibits sluggish electrochemical kinetics which is the detrimental role in triggering voltage fade and hysteresis. These findings point out a clear way to explore the relationship between voltage fade, hysteresis, and anionic redox. It also indicates that the irreversible oxygen release and oxygen redox reaction occur in the charging and discharging process of LR-NCMs, accompanied by the rearrangement and migration of TM ions in the TM layer to Li layer.^[11] This is the key to affect the electrochemical reaction rate and voltage attenuation of LR-NCMs. Identifying the cause of large voltage hysteresis and developing the strategy to overcome this issue is vital for developing high operating voltage LIBs. The majority of the research focuses on the structure-activity evolution of materials in the subsequent cycling process need to be conducted for practical applications. Meanwhile, the local oxygen environment, the local ordering of Li/TM in TM layers, and its impact on voltage curves need to be probed in detail. Another crucial matter that requires further exploration is how to manipulate and optimize these obstacles through structural and compositional design.

In this work, the formation processes of larger voltage hysteresis (larger lower voltage ($\approx 3.1 \text{ V}$) discharge capacity) have been analyzed and identified by electrochemical and structural

monitoring. The anionic/cationic redox sequence, structure evolution, TM ions migration and the electrochemical kinetic vary from oxidation to reduction process, resulting in path dependence and hysteresis. More importantly, we point out that the operating voltage and electrochemical kinetic of LR-NCMs can be effectively improved by manipulating and optimizing its local coordination structure by the lithium/oxygen (Li/O) ratio. Theoretical calculations verify that adjusting anionic redox chemistry by the Li/O ratio shifts the TM 3d—O 2p bands and the non-bonding O 2p band to a lower energy level, increasing the potential of redox reactions.

2. Results and Discussion

The as-prepared samples were synthesized by carbonate coprecipitation followed by annealing at 850 °C, demonstrated in our previous works.^[12] The HL (The as-prepared $\text{Li}_{1.20}\text{Mn}_{0.56}\text{Ni}_{0.16}\text{Co}_{0.08}\text{O}_2$ sample) particles are assembled from primary nano-particles, and the size of the secondary aggregate particle is 10–15 μm ; sizes are given in Figure S1a, Supporting Information. The local coordination structure of LR-NCMs is generally considered to be an aggregate of two local coordination structures (a layered monoclinic Li_2MnO_3 phase with C2/m space group and a layered hexagonal LiTMO_2 phase with R-3m space group), which is verified in Figure S1b,c, Supporting Information, and Figure 1a.^[5a,13] To explore the formation of the large voltage hysteresis of LR-NCMs, detailed electrochemical tests were conducted on the HL electrode at pre-activation, activation, and post-activation processes. First, the voltage window of the non-activated electrode is opened gradually with the upper cutoff voltage of 4.1, 4.3, 4.46, and 4.8 V, respectively. Charge/discharge curves and the corresponding dQ/dV plots are shown in Figure 1a,b. No obvious voltage hysteresis can be observed when the non-activated electrode was cycled with the upper cutoff voltage of 4.1 and 4.3 V. Only one peak can be observed in the corresponding dQ/dV plots during oxidation/reduction process, corresponding to the fast cationic redox ($\text{Ni}^{2+/3+/4+}$ and $\text{Co}^{3+/4+}$) without any voltage hysteresis.^[14] The voltage hysteresis is starting from 4.46 V, where the activation of Li_2MnO_3 component begins, introducing the oxygen redox. There are obvious differences in the charge/discharge path. After the activation process (4.8 V), the charge/discharge profiles display a large hysteresis and the discharge capacity is mainly distributed in low voltage region (below 3.4 V, a large peak can be observed during reduction process in Figure 1b).

To carefully monitor the formation of low-voltage capacity, detailed electrochemistry measurements were carried out on the HL electrode with a current of 20 mA g^{-1} . The cells of HL electrode were cycled at a 2.0–4.46 V (or 2.0–4.32 V) pre-activation cycle (1–20 cycles) and a 2.0–4.8 V activation cycle (21–25 cycles), followed by a 2.0–4.46 V (or 2.0–4.32 V) post-activation cycle (26–46 cycles). The results are displayed in Figure 1c,d and Figure S2, Supporting Information. There is no obvious voltage fade when HL electrode cycled in the voltage range of 2.0–4.32 V pre-activation cycle (1–20 cycles). However, the electrode cycled in the voltage range of 2.0–4.46 V shows a significant voltage fade, as shown in Figure 1c. The corresponding charge/discharge plots and dQ/dV plots of HL are illustrated

in Figure 1d. Since activation of the Li_2MnO_3 component in the as-prepared samples has not yet begun, only one peak at ≈ 4.0 V can be observed in dQ/dV curves in the 2.0–4.32 V pre-activation cycle (Figure S2, Supporting Information) or the initial cycle at a 2.0–4.46 V pre-activation cycle (Figure 1d). This is because this process predominantly involves the $\text{Ni}^{2+/3+/4+}$ or $\text{Co}^{3+/4+}$ redox states. There is no obvious change in the position of the dQ/dV peak after 20 cycles at 2.0–4.32 V and no peak observed at low voltage range in the dQ/dV curves. This is consistent with the change of average discharge voltage cycled at 2.0–4.32 V pre-activation cycle (No significant voltage drops, Figure S2, Supporting Information). This indicates that there was no activation of Li_2MnO_3 phase under this pre-activation process. As for the sample cycled at 2.0–4.46 V in the first 20 cycles, a small discharge peak appears at ≈ 3.1 V (Figure 1d red line) and the average discharge voltage decreased gradually due to the slow activation of Li_2MnO_3 phase in HL. In other words, the slow activation increased the low-voltage peak in dQ/dV plots. This means an increase in the low-voltage capacity eventually increased the entire discharge capacity, reducing the average discharge voltage (blue sphere in Figure 1c). This suggests that the formation of low-voltage capacity is closely related to the activation of Li_2MnO_3 phase. During the activation step (21st cycle) on the subsequent charge, the charging process has been divided into two steps: the first slope step in voltage plots involving the cationic redox under 4.4 V provided by LiTMO_2 phase, while the unique and distinguishable voltage plateau above 4.4 V (Figure 1d) stands for the release of oxygen and the extraction of Li-ions from the Li_2MnO_3 phase (the activation reaction of Li_2MnO_3 phase) induced by complicated chemical reaction and structure evolution.^[15] During the activation process of Li_2MnO_3 phase, anionic redox of LR-NCMs is activated, providing charge compensation and achieving higher capacities. At the same time, the activation step introduces a marked hysteresis in the charge and discharge profiles. A large peak (≈ 3.1 V) can be observed in dQ/dV curves after the activation cycle, which reduced the average discharge voltage (≈ 3.5 V) of the electrodes compared with the pre-activation cycle (≈ 4.0 V). This large peak (≈ 3.1 V) did not disappear during the post-activation cycle (26–46 cycles), which means that the activation reaction is accompanied by irreversible structural recombination.^[16] Interestingly, after the activation process, the average discharge voltage during the post-activation cycle (26–46 cycles) increases gradually (This will be discussed in Figure 2). From the above discussion, it can be concluded that the formation of low-voltage capacity and the reduction of operating voltage are closely related to the activation of the Li_2MnO_3 phase or the introduction of anionic redox. However, the effect of oxygen redox on the operating voltage and voltage hysteresis after activation is not yet understood, which needs further analysis.

Here, a series of fine electrochemical measurements were undertaken to evaluate the impact of the voltage window on the observed hysteresis, charge/discharge path and the mechanism of action on lithium storage performance. The voltage window of the activated electrode is opened gradually starting each cycle from 2.0 V. According to the position of the dQ/dV peak, the corresponding dQ/dV curves (Figure 2a) have been divided into three voltage ranges: Low voltage region (2.0–3.4 V), medium voltage region (3.4–4.1 V), and high voltage region (4.1–4.8 V).

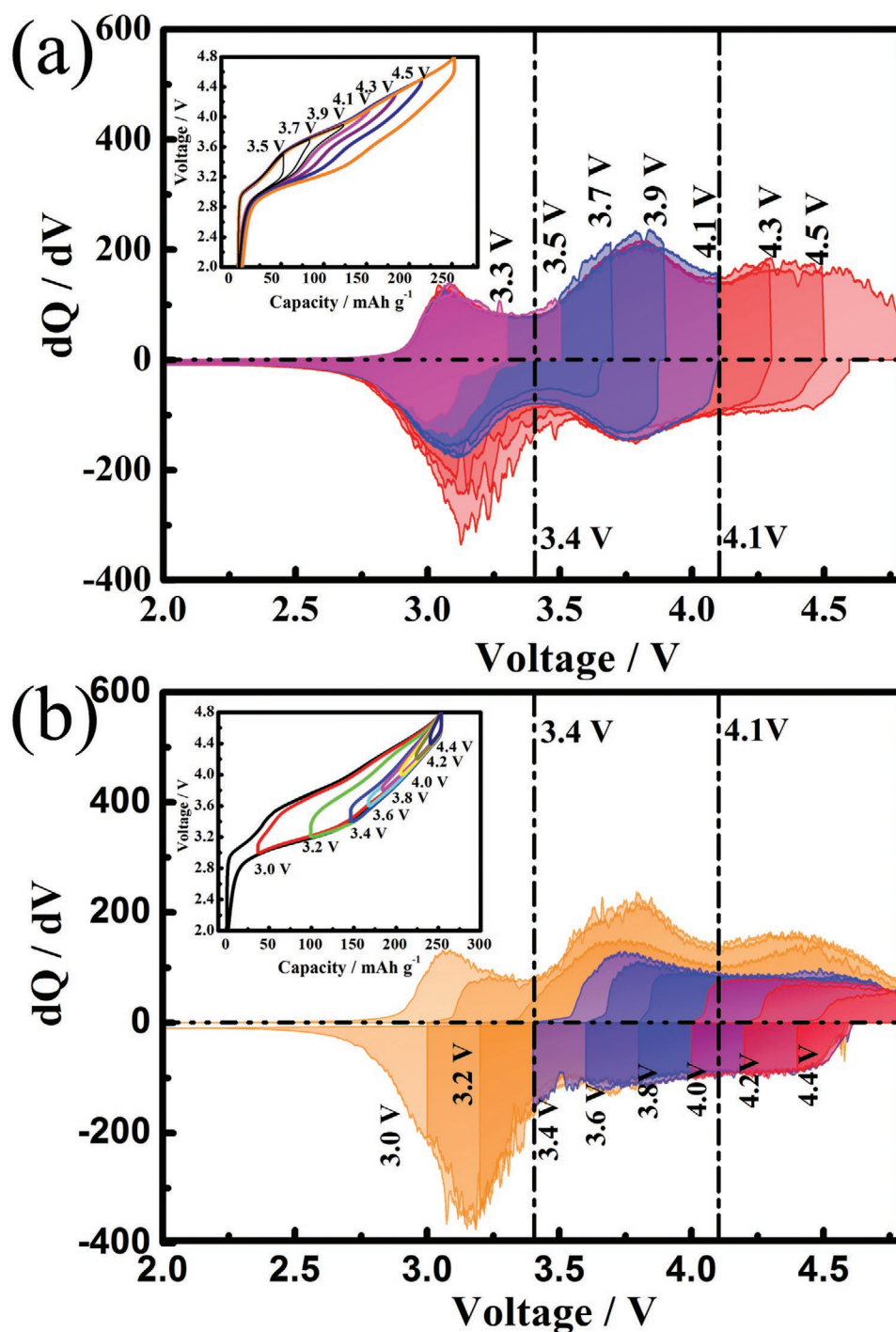


Figure 2. Effect of voltage window on the low-voltage capacity (voltage hysteresis). a) Voltage profiles (inset) and corresponding dQ/dV curves of HL electrode after activation cycles, as the charge voltage window is progressively increasing with each cycle beginning at 2.0 V. All curves in (a) start on the charge direction from 2.0 V and trace identical charging paths either, whereas the discharges vary with cutoff voltages. Different areas are highlighted with different colors. b) Voltage profiles (inset) and corresponding dQ/dV curves of HL electrode as the discharge window is progressively opened with each cycle beginning at 4.8 V with different lower voltage cutoffs, in a fashion opposite the first experiment. All curves in (b) start on the discharge direction from 4.8 V (fully charged initially).

When the charge cutoff voltage is lower than 3.4 V (Figure 2a, in the pink area), the main redox couple is $Mn^{3+/4+}$ and $Mn^{4+/3+}$ to provide charge and discharge capacity.^[17] The oxidative capacity below 4.1 V (in the pink and blue area) involves the redox couples

of $Mn^{3+/4+}$ and $Ni^{2+/4+}/Co^{3+/4+}$. Among them, the reduction of $Mn^{4+/3+}$ couple prevailing occurs in the low voltage region (pink area), while the reduction of $Ni^{4+/2+}/Co^{4+/3+}$ couple is split into both of the two regions: Low and medium voltage regions

(blue area). This increases the low-voltage capacity and causes partly voltage hysteresis. Furthermore, the cationic oxidation is nearly completed before charging with 4.1 V. This implies that the oxidation peak of dQ/dV above 4.1 V is mainly affected by anionic oxidation.^[7d,b,15b] A large hysteresis occurs in reductive capacity due to the reduction reaction of the oxidic O^{n-} which occurs at two voltage regions: high (above 4.1 V) and low voltage (below 3.6 V) region. This causes a difference in the charge/discharge path. Each color in Figure 2a roughly represents a redox pair: pink for $Mn^{3+/4+}$, blue for $Ni^{2+/4+}/Co^{3+/4+}$, and red for $O^{2-/n-}$. Based on the characteristics of different redox reactions and the analysis of electrochemical window test results, the hysteresis low-voltage reductive capacity at 2.0–3.4 V can be roughly analyzed through different color-area ratios (displayed in Figure 5h), where about 35.2% is provided by the reduction of $Mn^{4+/3+}$, 27.5% by lagging reduction of $Ni^{4+/2+}/Co^{4+/3+}$, and 37.3% by lagging reduction of $O^{n-/2-}$. Next, in the complementary experiment, the discharge voltage window is generally opened, starting each cycle from 4.8 V. This further confirms the above conclusion. The low-voltage reductive capacity (below 3.4 V) is oxidized throughout charging at 2.0–4.8 V (Figure 2b, the area in orange). Based on the above conclusions, the average discharge voltage increases gradually during the post-activation cycle (no matter at voltage of 2.0–4.32 or 2.0–4.46 V) in Figure 1c and Figure S2, Supporting Information, mainly due to the incomplete anionic oxidation reaction. All in all, the complete anionic oxidation reaction during the activation cycle (at 2.0–4.8 V) introduced a large low-voltage capacity (≈ 3.1 V, reduction of $Mn^{4+/3+}$, lagging reduction of $Ni^{4+/2+}/Co^{4+/3+}$ and $O^{n-/2-}$) in the reduction reaction process. In the post-activation cycle, only partial oxygen is involved in the oxidation reaction, reducing the low-voltage capacity (≈ 3.1 V, contributed by lagging reduction of $O^{n-/2-}$) in the reduction reaction process (The peak located in 3.8 V exhibits no significant change). As a result, the average discharge voltage increased. Moreover, the huge voltage hysteresis and the differences in the charge/discharge path can also reflect structural rearrangement of the active materials during charging and discharging. This may affect the site energies of the sample structure and the relative ease by which lithiation–delithiation reactions occur.

To further unveil the lithiation–delithiation mechanism in activated LR-NCMs during cycling, ex situ X-ray diffraction (XRD) and Raman were performed for the selected electrodes after activation during the cycling process, displayed in Figures 3 and 4 and Figure S3, Supporting Information. Figure 3a shows a typical charging and discharging voltage profile. Figure 4b,d show the corresponding dQ/dV plot of an HL cell when cycled between 2.0 and 4.8 V at 25 mA g^{-1} (sixth cycle shown). The points marked in Figure 3a and Figure 4b,d indicate the representative ex situ electrodes where the XRD data was collected.

The ex situ XRD data of the selected electrodes can be fitted to the hexagonal unit cell by GSAS+EXPGUI suite for convenience due to the similarity between Li_2MnO_3 and $LiTMO_2$ in structure.^[11b,18] Figure 3b shows the (003) peak of those ex situ electrodes in Figure 3a. The results of fitting are displayed in supporting information Table S2, Supporting Information. Figure 3d shows the schematic of the crystal structure of $LiTMO_2$ and the corresponding lattice parameters of

a , c , $d(O-O)$ and $\alpha(O-TM-O)$. The lattice parameter a represents the average of interlayer O-O distance or nearest neighbor distance of TM-TM in the TM planes, while the lattice parameter c corresponds to the average interlayer distance between the close-packed oxygen planes, as seen in Figure 3e.^[9] In Figure 3c, the black line shows the evolution of parameter a where gradually decreases during the charging step and comes back during the discharging step, but the path varies from charging to discharging. The decreased parameter a during the charging process means the decrease in TM ionic radii in TM layer, caused by the oxidizing of TM ions. From the change of parameter a , the valence state of TM ions can also be inferred. Its different slopes in each region indicate a different redox process. It is clear that the obvious different variation rates of parameter a indicate different electrochemical reaction paths for charging and discharging, resulting in the differences of charge/discharge path. Meanwhile, the evolution of parameter c also varies from charging to discharging. The peak position of (003) in Figure 3b changes regularly during charging and discharging, which can directly reflect the evolution of c of the sample and also represent reversible Li-ion insertion–extraction during cycling. Therefore, this can be used for further research related to the phase transformation mechanism during cycles. At the beginning of charging, (003) peak first shifts to the left (means the increase of the $d_{(003)}$ -spacing) and then gradually shifts back till the end of charging. This corresponds to the evolution of the interlayer lattice parameter c increased first until 4.1 V and then decreased. The expanding of c and $d_{(003)}$ -spacing during charge to ≈ 4.1 V due to the increased of the electrostatic repulsion between oxygen slabs when the Li^+ extract from the Li-layers. And then lattice parameter c contracts until the top of charge (≈ 4.8 V). This is because of the extraction of Li^+ from the TM slabs and the migration of TM ions, ultimately leading the inverse changes of unit cells and shifting (003) peak to higher reflection angles. As the reverse process occurs during discharge, the interlayer spacing expands first before shrinking to its original value (when discharged to 2.0 V).^[7a,19,20] In the process of refining these XRD data, the regularity of $d(O-O)$ and $\alpha(O-TM-O)$ along c axis (as shown in Figure 3e) has caught our attention. The $d(O-O)$ and $\alpha(O-TM-O)$ along c axis gradually decrease during the charging step, indicating that the distance between the two oxygen is continuously decreasing during the delithiation process. The decreasing distance can be attributed to the oxidation of TM or the formation of peroxy O-O dimers. Unlike the charging process, the change of $d(O-O)$ and $\alpha(O-TM-O)$ along c axis in the discharge process are divided into two processes. The $d(O-O)$ and $\alpha(O-TM-O)$ along c axis first changes slowly and then increases sharply (2.643 Å and 85.39° for D-11, 2.778 Å and 88.06° for D-12), indicating the different electrochemical reaction processes. Such asymmetric vary in structure evolution (lattice parameters of a , c , $d(O-O)$ and $\alpha(O-TM-O)$) during charging and discharging may have a critical effect on the voltage profiles, resulting in a voltage hysteresis. All the results demonstrate that the evolution of the structure of activated LR-NCMs has certain reversibility during charging and discharging, although there are some minor structural lags in the behavior of a and c in Figure 3c.

To further confirm the variation of the micro-structure of activated LR-NCMs material during the charging and discharging,

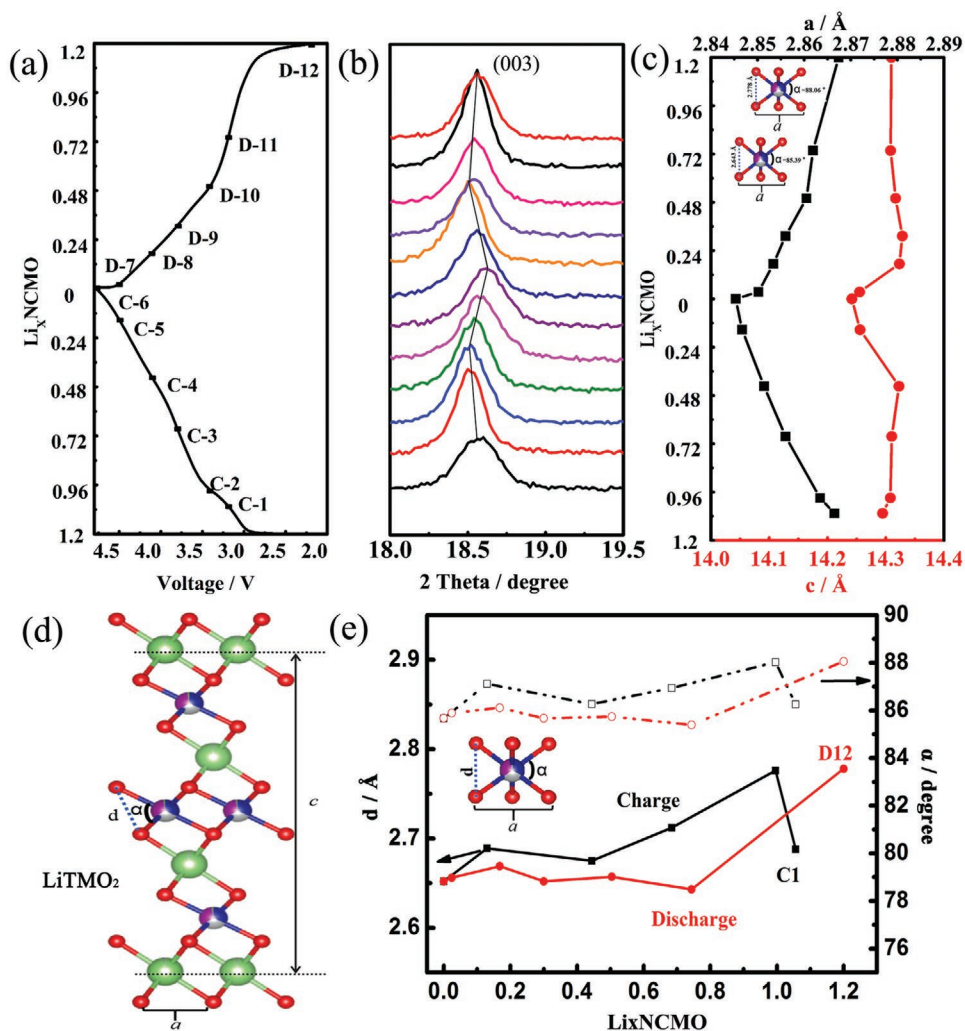


Figure 3. a) The charge/discharge curve for an HL cell cycled between 2 and 4.8V at 25 mA g⁻¹ and room temperature after 5 activation cycles. b) Ex situ XRD data for HL electrodes at various state of charge and discharge, the (003) peaks refer to R-3m symmetry, for simplicity. c) Variation of *a* and *c* cell parameters during ex situ charge and discharge of the activated HL electrodes. d) Schematic of the crystal structure of LiTMO₂ and the corresponding lattice parameters of *a*, *c*, *d*(O-O) and α (O-TM-O). e) The corresponding *d*(O-O) and α (O-TM-O) during ex situ charge and discharge of the activated HL electrodes. The black square points marked on (a) indicate the representative ex situ electrodes at which the XRD data was collected.

ex situ Raman spectroscopy has been applied because it is more sensitive to the short-range local structure. Figure 4a,c displays the ex situ Raman of the selected electrodes, which is mentioned in Figure 4b,d. Significant changes can be observed from the fitted peaks. Three main peaks are presented in the Raman spectrum (fitted peak 1, 2, 3). The first two Raman peaks, peak 1 and 2, can be attributed to the E_g and A_{1g} vibrations of the Raman-active layered structure, respectively. Whereas, peak 3 is associated with the spinel-like phase.^[18c,21] The A_{1g} band, peak 2, gradually decreases during charging steps compared to E_g , peak 1, due to the effects of changes in local symmetry (caused by lithium deintercalation) on the vibration of TMO_6 .^[22] At the reverse process occurring during discharge, the A_{1g} band, peak 2, gradually becomes apparent compared to E_g , peak 1. The evolution of peak 3 indicates the change of spinel-like phase content in the electrode under different voltages. The spinel structure in the electrode was gradually increased as the peak 3 proportion increased before being charged to 4.1 V. Afterwards

the peak 3 proportion slightly reduced. These results indicate that the TM ions gradually migrate out of the TM layer to form the spinel structure during the cationic oxidation process (2.0–4.1 V). During the anionic oxidation process (>4.1 V) TM ions partially migrate back to their previous state.^[23] Meanwhile, the peak 3 proportion will decrease during discharge steps, indicating that the reversible TM ions migrated back to the previous state. The Raman data further proves the existence of reversible migration of TM ions during charging and discharging. Such asymmetric changes and migration of TM ions during charge and discharge process may be the cause of different charge-discharge paths and voltage hysteresis. What's more, during long cycles, the frequent migration of TM ions increases the risk of TM ions trapped in the intermediate tetrahedron, which may be one of the causes of the capacity and voltage fade.

To further clarify the electrochemical kinetics of activated LR-NCMs electrodes, the electrochemical impedance spectroscopy (EIS) Nyquist plots and galvanostatic intermittent titration

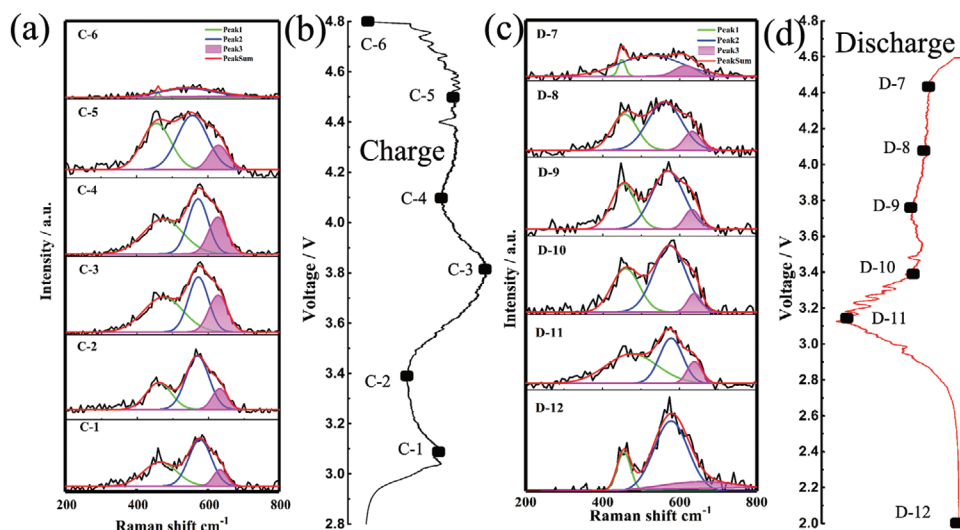


Figure 4. Ex situ Raman data of HL electrodes for the selected points during a) charge and c) discharge process. The corresponding dQ/dV curve of b) charging and d) discharging. The black square points marked on (b,d) indicate the representative ex situ electrodes at which the Raman data were collected.

technique (GITT) curves during charging and discharging after 5 activation cycles in the range of 2.0–4.8 V at 25 mA g⁻¹, are given in **Figure 5** and Figures S4 and S5, Supporting Information. The oxidation/reduction processes were divided into three voltage ranges (low voltage region: 2.0–3.4 V, medium voltage region: 3.4–4.1 V and high voltage region: 4.1–4.8 V) and to compare the transport properties of each voltage region at the same electrode. All parameters remain the same due to the same electrode. As a function of voltage, cell resistance (including R_{hf} representing interphase contacts and surface film, etc., and R_{ct} signifying interfacial charge-transfer) exhibits different trends on charging and discharging paths (Figure 5a,c–f), which emphasizes path dependency. R_s represents the solution resistance, which has no obvious change in a charge-discharge cycle (Figure 5d). However, when R_{hf} as a function of voltage is observed, some conclusions can be drawn. With the deepening of charging and discharging, the impedance is increasing (Figure 5e), which may be one of the causes that make the capacity and voltage fade. As for R_{ct} (Figure 5f), it is known that it is quite large at both low and high voltage regions, especially at high voltage region (above 4.1 V). This indicates that the internal resistivity is much higher during the oxygen redox process.^[24] Interestingly, R_{ct} undergoes a higher impedance at 3.4 V compared to 3.0 or 3.8 V during either oxidation or reduction processes. These results are consistent with the lower D_{Li^+} (pseudo or apparent Li⁺ diffusion coefficients) at 3.4 V calculated from GITT results (Figure 5g,h), detailed calculation processes are shown in support information Figure S5, Supporting Information. The kinetics is fastest in the middle voltage region with low R_{ct} and high D_{Li^+} during either charging or discharging, which falls in the cationic Ni^{2+/4+}/Co^{3+/4+} redox potential range discussed in Figure 2. Meanwhile, the high R_{ct} and low D_{Li^+} at the high voltage illustrate the slower kinetics of anionic O^{n-/2-} redox. To sum up, the cationic redox has faster kinetics than anionic redox. Furthermore, the D_{Li^+} is much lower in discharging below approximately 3.6 V

than in charging (Figure S5, Supporting Information), where the lagging reduction of O^{n-/2-} began (red area in Figure 5h). This means that the lagging anionic redox reduced the corresponding kinetics in that region. This further confirms the existence of anionic redox at the low voltage region. The low D_{Li^+} value of about 3.4 V may indicate the boundary of the different electrochemical reaction processes, and the real reason for that is still unclear. The underlying reason still requires extensive research.

The dQ/dV curve of activated LR-NCMs consists of several dQ/dV peaks, which we have now redistributed in combination with spectroscopic and electrochemical evidence, as summarized in Figure 5h. As discussed above, each color region roughly represents the capacity provided by a type of redox pair, and the corresponding D_{Li^+} represents the diffusion kinetics of lithium ions in different electrochemical reactions. Cationic redox with faster kinetics occurs at 3.8 V (Ni^{2+/4+}/Co^{3+/4+}, blue area) and at about 3.2 V (Mn^{3+/4+} in pink area, lagging Ni^{2+/4+}/Co^{3+/4+} in the blue area) during the charge/discharge process. As for anionic redox, it occurs asymmetrically during charging and discharging. The anionic redox mainly occurs at above 4.1 V during the oxidation process. During the reduction process, some of the anion reduction reactions occur at high voltage, while others occur at a much lower voltage (peak below 3.6 V). Meanwhile, the anionic redox with lower kinetics reduces the lithium ions diffusion below 3.6 V during discharging contrary to charging (Figure S5, Supporting Information). It is now clear, as discussed above, the anionic/cationic redox sequence, structure evolution, TM ions migration and the electrochemical kinetic vary from oxidation to reduction process, resulting in path dependence and hysteresis.

Based on the above theory, it is known that by adjusting the redox of anions and cations, the operating voltage and kinetics, as well as voltage hysteresis, can be manipulated. As discussed in the Introduction, anionic redox chemistry in LR-NCMs is mainly caused by these pure non-bonding 2p states (generated by the

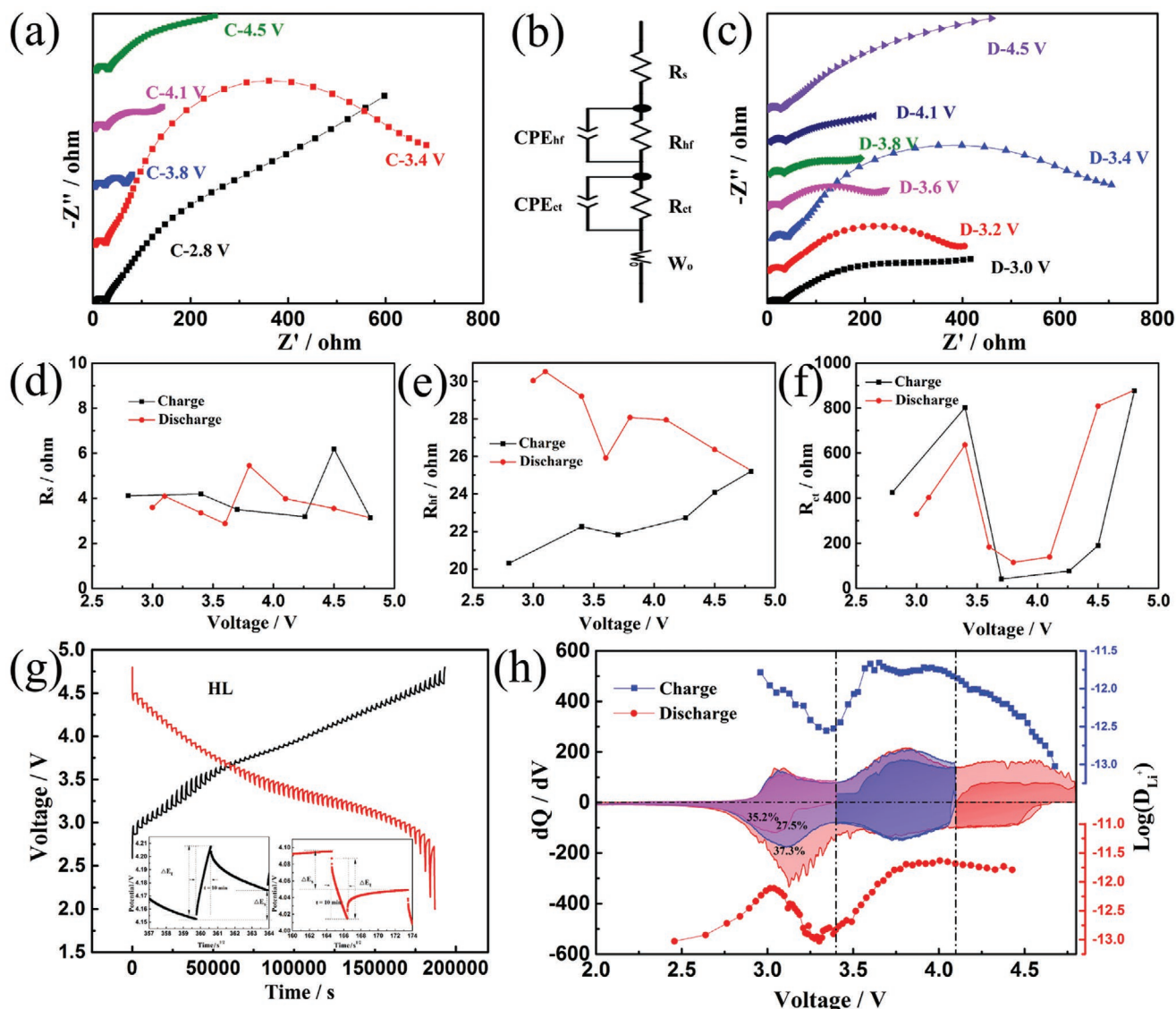


Figure 5. Electrochemical kinetics were tested for activated HL after 5 activation cycles in the range of 2.0–4.8 V at 25 mA g⁻¹; Impedance is measured at each step after the sixth rest. For convenience, each step impedance is represented by a C-voltage, or a D-voltage (e.g., C-3.8 V represents the impedance test when charging to 3.8 V, D-3.8 V represents the impedance test when discharging to 3.8 V). The evolutions of HL electrode EIS Nyquist plots are shown for a) charge and c) discharge. d) R_s , e) R_{hr} , and f) R_{ct} determined by fitting the spectra utilizing the equivalent circuit. b) The corresponding equivalent circuits for HL electrode. GITT curves of HL g) during the sixth charging/discharging process, the single titration shows a straight line behavior between $t^{1/2}$ and V for HL electrode in illustration. h) Summary of activated LR-NMC's charge-compensation mechanism and electrochemical kinetics and the relationship between Li-ion diffusion coefficient and the potential based on GITT analysis. Key dQ/dV curves from voltage window opening experiments in Figure 2 and the capacity analysis in different voltage ranges of HL are overlapped with each other, keeping the same colors as before.

Li-O-Li configurations), which can be tuned by modulating cation arrangement or local oxygen structure.^[25] In this paper, we also try to manipulate the voltage feature of LR-NMCs by tuning anionic redox reactions (local oxygen environment). To better understand the relationship between local structure and anionic redox and the electrochemical feature, the LR-NMCs with different Li/O ratio are studied. First, we compared the initial charge/discharge curves and dQ/dV plots of LR-NMCs samples with different Li/O ratio, as shown in Figure 6a,b. It was determined that the discharge curves of samples show significant differences. A lower operating voltage is evident with the increase

of the Li/O ratio, despite no obvious difference in charging curves. What is more, the higher Li/O ratio in the crystal lattice, the lower coulombic efficiency there are (inset of Figure 6a).^[26] Interestingly, the value of dQ/dV reduction peak at high voltage (≈ 3.7 V) is decreasing. However, at low voltage (≈ 3.1 V), it is increasing with the Li/O ratio in the crystal lattice (except sample Li_{1.26}). The details of the electrochemical performance and discussion of those electrodes are displayed in Figure S6, Supporting Information. All these results indicate that the operating discharge voltage decreased and the low-voltage capacity (≈ 3.1 V) increased with the increase of the Li/O ratio in the crystal lattice,

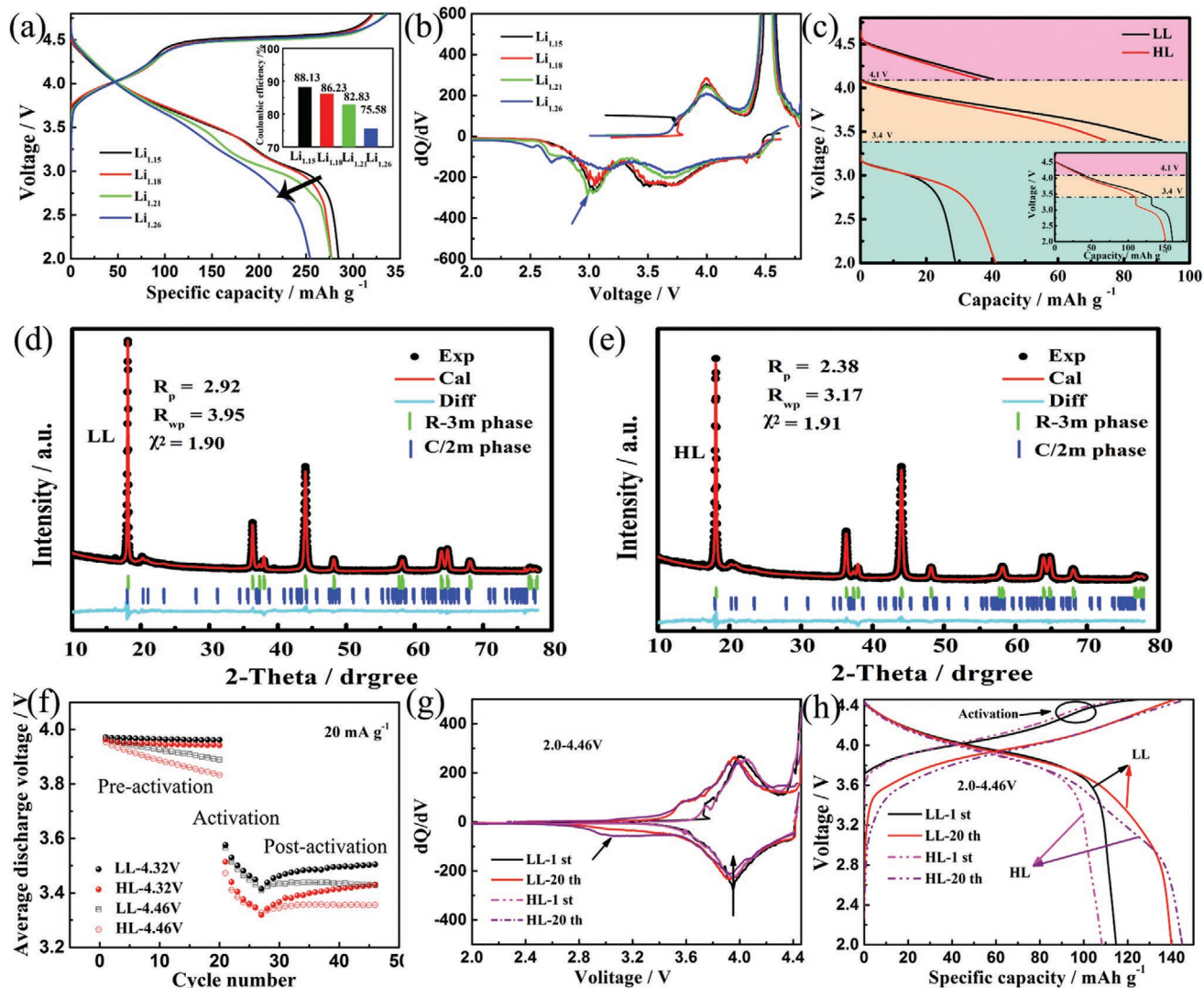


Figure 6. a) The initial charge/discharge plots, initial coulombic efficiency in the illustration and b) differential capacity plots of the as-prepared samples measured at a 0.1 C rate in the potential range of 2.0–4.8 V. c) Capacity analysis in different voltage ranges (4.8–4.1, 4.1–3.4, and 3.4–2.0 V) of HL and LL, after 5 cycles at a 0.1 C activation. The observed refinement results of d) LL and e) HL. The calculated patterns are shown by solid curves, and the black dots show the observed intensities, and the differences between the observed and calculated intensities are presented by cyan curves. f) Average discharge voltage of LL and HL cycled in different voltage ranges (2.0–4.32, 2.0–4.46 V). g) charge/discharge plots and h) dQ/dV versus for the first 20 cycles of LL and HL along with the slow activation of Li₂MnO₃ phase.

which means that the structure of LR-NCMs can be manipulated by Li/O ratio based on the above discussions. The XRD patterns and the results of the Rietveld refinement can also prove these results, which are shown in Figure 6d,e and Table S3, Supporting Information. Compared to the weight fraction of layered monoclinic Li₂MnO₃ phase (≈ 46.99 wt%) and hexagonal LiTMO₂ phase (≈ 53.01 wt%) in LL (Li_{1.18} sample), the HL sample exhibits higher Li₂MnO₃ weight fraction of 48.66 wt% and lower LiTMO₂ weight fraction of 51.34 wt%. These weight fractions are consistent with expectations of compositional phases. Lower Li/O ratio in LL exhibits lower Li-O-Li configurations than HL. This implies a higher anionic redox ratio in HL exists. These results indicate that Li/TM ordering in TM layers of LR-NCMs can be manipulated by Li/O ratios. By adjusting the Li/O ratio, the local oxygen environment (anionic redox) in LR-NCMs can also be tuned.

Furthermore, to better understand the capacity distribution of HL and LL in different voltage ranges, the charge–discharge process has been artificially divided into three voltage intervals: 2.0–3.4 V, 3.4–4.1 V, 4.1–4.8 V (as above discussion in Figure 2). The capacity analysis in different voltage ranges after 5 cycles at a 0.1 C activation is illustrated in Figure 6c. Evidently, the capacity of LL is higher than HL in the high voltage range of 3.4–4.1 and 4.1–4.8 V, and lower than HL in the low voltage range of 2.0–3.4 V. Combining with the XRD results, it shows that a higher anionic redox ratio in HL compared to LL, results in a higher low-voltage capacity (below 3.4 V), and the lower operating voltage available. These findings are consistent with the above discussions. Detailed electrochemistry measurements were also tested on LL electrodes using 20 mA g⁻¹, the same as above tested on HL electrode (Figure 1c). The results

of the LL electrode shown in Figure 6f,g and Figure S7, Supporting Information, are consistent well with that of HL electrode discussed in Figure 1. Figure 6f shows the average discharge voltage of LL and HL cycled at different activation processes. First, the average discharge voltage of LL electrodes (no matter cycled in the voltage range of 2.0–4.32 or 2.0–4.46 V) is always higher than that of HL electrodes. From the initial charge/discharge curves in Figure 6h, the activation voltage of the HL electrode is lower than the LL electrode. Meanwhile, the initial capacity of the LL electrode is higher than that of HL electrode, but the capacity after 20 cycles of LL is lower than that of HL. This means the activation of HL is faster than that of LL. It can also be seen in Figure 6g that the low-voltage peak (≈ 3.1 V) of HL is higher than that of LL after 20 cycles, which lowers the operating voltage of the electrode. These results indicate that the activation of Li_2MnO_3 in the HL electrode is easier to occur than in the LL electrode. The electrodes cycled at 2.0–4.46 V during the first 20 cycles experiences a small discharge peak that appears at ≈ 3.1 V. Also, the average discharge voltage decreased gradually due to the slow activation of the Li_2MnO_3 phase in LL and HL. Meanwhile, to verify the accuracy of kinetics characteristics, the same EIS and GITT tests were conducted on the LL electrode, shown in Figures S8 and S9, Supporting Information. All the results are consistent well with that of HL electrode in Figure 5. This means that our experiments and results are not accidental. Besides, compared with HL electrode, the LL electrode possesses higher kinetics due to the lower anionic redox contribution (Figure S8, Supporting

Information). Combined with the discussion above, the structure of LR-NCMs can be finetuned by the Li/O ratio, and eventually tune the anionic redox activity. This ultimately leads to the improvement of electrochemical properties.

Density functional theory (DFT) calculations are also performed to investigate the effect of the Li/O ratio on structural and electrochemical characteristics of LR-NCMs. Model supercells, $\text{Li}_{15}\text{Mn}_7\text{Ni}_1\text{Co}_1\text{O}_{24}$ (Represents HL in Figure 7c, the red line in Figure 7e,f) and $\text{Li}_{13}\text{Mn}_7\text{Ni}_2\text{Co}_2\text{O}_{24}$ (Represents LL in Figure 7d, the black line in Figure 7e,f) were selected to explore the effect of different Li/O ratio on the projected densities of states of the O 2p and TM 3d states, which are shown in Figure 7a,b. First, it is known that the pure non-bonding O 2p states (which will introduce anionic redox chemistry) will be generated along with Li-O-Li configurations. As displayed in Figure 7c,d, the red regions are Li-O-Li configurations, which means there is a higher content of Li-O-Li configurations in HL samples than that in LL samples (seen in the discussion of XRD patterns in Figure 6). Compared to HL, the band of non-bonding O 2p and TM 3d—O 2p of LL exhibits a lower energy level, as displayed in Figure 7c,d. The redox voltage is determined by the energy gap between electrons participating in redox reaction (no matter for the 3d-electrons of the TM ions, or the 2p-electrons of the oxygen ions) and the Li^+/Li^0 energy level. The previous reports^[25b,27] stated that lower energy represents a higher redox potential. Thus, by adjusting the Li/O ratio, the band of non-bonding O 2p and TM 3d—O 2p is lowered successfully in LR-NCMs, resulting in higher redox reaction

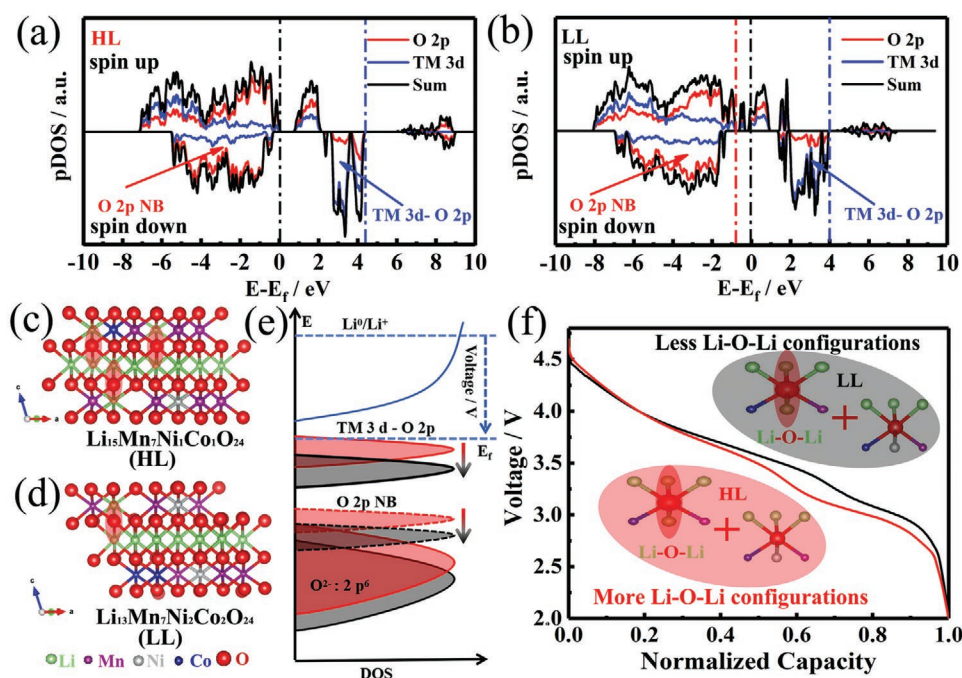


Figure 7. The projected density of states (pDOS) of the O 2p orbitals of O atoms and the TM 3d orbitals of TM atoms in a) $\text{Li}_{15}\text{Mn}_7\text{Ni}_1\text{Co}_1\text{O}_{24}$ (HL) and b) $\text{Li}_{13}\text{Mn}_7\text{Ni}_2\text{Co}_2\text{O}_{24}$ (LL). Schematic electronic structures for c) $\text{Li}_{15}\text{Mn}_7\text{Ni}_1\text{Co}_1\text{O}_{24}$ (HL) and d) $\text{Li}_{13}\text{Mn}_7\text{Ni}_2\text{Co}_2\text{O}_{24}$ (LL). e) Schematic diagram of the electronic structure in different electrode material (Red line for HL and black line for LL), according to the above pDOS. The above solid line is the TM 3d—O 2p band, and the below-dashed line is the O 2p non-bonding (O 2p NB, Li-O-Li geometry) structure of samples, while the energy of black line (LL) is lower than that of the red line (HL). f) The normalized capacity versus potential curves of the cathode materials with different local coordination structures at 0.1 C, room temperature and voltage range of 2.0–4.8 V (Illustration: The local oxygen environment of HL (red region) and LL (black region) sample).

potential, shown in Figure 7e. This is consistent with the electrochemical results in Figure 7f. Besides, the voltage features of pure monoclinic (Li_2MnO_3) and rhombohedral phases were also explored in Figure S10, Supporting Information. Lower Li/O ratio in LR-NCMs with less Li-O-Li configurations possess a higher voltage curve. As described above, regulating the Li/O ratio in the material will be a simple yet effective strategy to adjust the local electronic structure of the material, leading to decreased configurations of Li-O-Li. This yields smaller contributions of oxygen redox, ultimately improving the operating voltage and kinetics to a certain extent.

3. Conclusion

Voltage hysteresis is an undesirable characteristic of LR-NCMs. Understanding what factors trigger or alleviate voltage hysteresis is vital for developing high energy LIBs. In this work, the formation process of voltage hysteresis has been probed in detail and identified by electrochemical and structural monitoring. The special Li-O-Li configurations which trigger anionic redox chemistry in LR-NCMs have a close relationship with the low operating voltage and lower-voltage capacity (≈ 3.1 V). Meanwhile, the anionic/cationic redox sequence, structure evolution, and TM ion migration, which determines the voltage profile of LR-NCMs, vary from oxidation to reduction processes, resulting in path dependence and hysteresis. More importantly, a simple yet effective strategy has been proposed that fine-modulating local oxygen environment by altering the Li/O ratio, which can tune the anionic redox chemistry. This eventually improves its electrochemical properties, including the operating voltage and kinetics, etc. DFT calculations verify that adjusting anionic redox chemistry by changing the Li/O ratio shifts the TM 3d -O 2p bands and the non-bonding O 2p band to a lower energy level, resulting in higher redox reaction potential. Our work provides guidelines for understanding, manipulating and optimizing the complex chemical composition of cathodes, which may unlock more information and advancements relevant to designing high-energy-density layered cathodes.

4. Experimental Section

Material Synthesis: LR-NCMs samples were prepared by carbonate coprecipitation and a solid-state method.^[12b] Stoichiometric TM carbonate ($\text{Ni}_x\text{Co}_y\text{Mn}_{1-x-y}\text{CO}_3$) was obtained by co-precipitation reaction of TM sulfates ($\text{NiSO}_4 \cdot 6\text{H}_2\text{O}$, $\text{CoSO}_4 \cdot 7\text{H}_2\text{O}$, and $\text{MnSO}_4 \cdot 6\text{H}_2\text{O}$, 2 M) aqueous solutions and the mixed Na_2CO_3 (2 M) and $\text{NH}_3 \cdot \text{H}_2\text{O}$ (0.2 M) aqueous solution. The mentioned mixed solution was carried out under controlled conditions (pH = 7.5, T = 55 °C, stirring speed = 1000 rpm min^{-1}), using a continuously stirred tank reactor and standing 15 h to confirm the morphology and homogeneity of particles. The obtained TM carbonate powders were mixed and ground with a different molar ratio of Li (LiCO_3) to TM. This result was then heated at 500 °C for 5 h and 850 °C for 12 h to obtain the LR-NCMs powders, named $\text{Li}_{1.15}$, $\text{Li}_{1.18}$ (LL), $\text{Li}_{1.21}$ (HL), and $\text{Li}_{1.26}$.

Material Characterizations: The elemental analysis of LL and HL was carried out by inductively coupled plasma-optical emission spectroscopy (Thermo Scientific iCAP6300, U.S.A). The results, reported in Table S1, Supporting Information, show that the technological composition of each metal is close to the stoichiometry. The crystal structure of the samples was characterized by XRD (a Rigaku-D/MAX-2500/pc with

Cu Ka radiation), and Rietveld refinements of the XRD pattern obtained by GSAS+EXPGUI suite by using a layered monoclinic Li_2MnO_3 phase and a layered hexagonal LiTMO_2 phase as a model. General data for the Rietveld analysis was collected by a step-scan method with measurement conditions: $2\theta = 10\text{--}80^\circ$, 2 s per step, and 0.02° per step. Local structures of the samples were studied by Renishaw inVia Raman microscope with a laser of 532 nm wavelength and power of 150 μW . The morphologies of as-prepared samples were investigated using a scanning electron microscope (S-4800, Hitachi, Japan, operated at 10 kV). Theoretical calculations were carried out using the CASTEP module of Materials Studio software package^[28] within the DFT framework. Supercells of $\text{Li}_{15}\text{Mn}_7\text{Ni}_1\text{Co}_1\text{O}_{24}$ and $\text{Li}_{13}\text{Mn}_7\text{Ni}_2\text{Co}_2\text{O}_{24}$ were selected to represent HL and LL, respectively. Detailed information was shown in the Supporting Information Computational Details.

Electrochemical Measurements: All electrochemical tests were conducted by assembling coin-type half-cells with Li metal negative electrode. The counter electrode was a homogeneous mixture with a mass ratio of 8 (LR-NCMs):1 (Super P):1 (polyvinylidene fluoride). In this report, the average mass loading of the active cathode materials on the aluminum foil averaged to 4.0 mg cm^{-2} . A microporous polypropylene film (Celgard 2400) was used to separate positive and negative electrodes. Also, 1 M LiPF_6 dissolved in ethylene carbonate:propylene carbonate:dimethyl carbonate (DMC) in a 1:1:1 weight ratio was used as the electrolyte. All cells were left for 12 h and then tested. The cells were tested by galvanostatic charge/discharge cycling on a battery testing system at 25 °C. The cyclic test was performed at 1 C (250 mA g^{-1}) at 2.0–4.8 V. During GITT testing, a constant current flux of 25 mA g^{-1} for a given period (10 min) was supplied, followed by open-circuit conditions for 40 min. EIS was measured by an electrochemical workstation (CHI660E). EIS was recorded by applying an AC voltage of 5 mV in the frequency range from 10^5 to 10^{-2} Hz. After the fifth activation cycle, the desired SOC was achieved using a constant current density of ± 25 mA g^{-1} . Once the desired SOC was obtained the cells were disassembled in the glovebox carefully. The positive electrode powders were rinsed thoroughly three times with anhydrous DMC to get rid of the electrolyte and soluble surface deposits. DMC was evaporated by leaving the samples in the glovebox for at least 12 h.

Supporting Information

Supporting Information is available from the Wiley Online Library or from the author.

Acknowledgements

G.S. and F.-D.Y. contributed equally to this work. G.S. acknowledges financial support from the Chinese Scholarship Council (CSC). The authors also acknowledge the financial support from the National Natural Science Foundation of China (Grant No. 51674221, 51704261, and 51902072) and China postdoctoral science foundation (Grant No. 2017M621285 and 2018T110292) and the Natural Science Foundation of Hebei Province (B2018203330 and B2018203360).

Conflict of Interest

The authors declare no conflict of interest.

Keywords

anionic redox, Li- and Mn-rich cathodes, Li-ion batteries, Li-poor materials, voltage hysteresis

Received: March 23, 2020

Revised: August 19, 2020

Published online:

- [1] a) B. Obama, *Science* **2017**, *355*, 126; b) M. Armand, J. M. Tarascon, *Nature* **2008**, *451*, 652; c) B. Ammundsen, J. Paulsen, *Adv. Mater.* **2001**, *13*, 943.
- [2] a) W. Liu, P. Oh, X. Liu, M. Lee, W. Cho, S. Chae, Y. Kim, J. Cho, *Angew. Chem.* **2015**, *127*, 4518; b) M. S. Whittingham, *Chem. Rev.* **2004**, *104*, 4271; c) G. Sun, X. Yin, W. Yang, J. Zhang, Q. Du, Z. Ma, G. Shao, Z. Wang, *Electrochim. Acta* **2018**, *272*, 11; d) J. Song, B. Sun, H. Liu, Z. Ma, Z. Chen, G. Shao, G. Wang, *ACS Appl. Mater. Interfaces* **2016**, *8*, 15225.
- [3] a) X. Yu, Y. Lyu, L. Gu, H. Wu, S. Bak, Y. Zhou, K. Amine, S. N. Ehrlich, H. Li, K. Nam, X. Yang, *Adv. Energy Mater.* **2014**, *4*, 1300950; b) Y. Xie, M. Saubanère, M. L. Doublet, *Energy Environ. Sci.* **2017**, *10*, 266; c) J. Zheng, S. Myeong, W. Cho, P. Yan, J. Xiao, C. Wang, J. Cho, J. Zhang, *Adv. Energy Mater.* **2017**, *7*, 1601284; d) T. Yi, Y. Li, S. Yang, Y. Zhu, Y. Xie, *ACS Appl. Mater. Interfaces* **2016**, *8*, 32349; e) F. Yu, L. Que, C. Xu, M. Wang, G. Sun, J. Duh, Z. Wang, *Nano Energy* **2019**, *59*, 527; f) S. Hu, A. S. Pillai, G. Liang, W. K. Pang, H. Wang, Q. Li, Z. Guo, *Electrochem. Energy Rev.* **2019**, *2*, 277.
- [4] a) M. Sathiya, A. M. Abakumov, D. Foix, G. Rousse, K. Ramesha, M. Saubanère, M. L. Doublet, H. Vezin, C. P. Laisa, A. S. Prakash, D. Gonbeau, G. VanTendeloo, J.-M. Tarascon, *Nat. Mater.* **2015**, *14*, 230; b) S. Hy, F. Felix, J. Rick, W. Su, B. J. Hwang, *J. Am. Chem. Soc.* **2014**, *136*, 999.
- [5] a) D. Seo, J. Lee, A. Urban, R. Malik, S. Kang, G. Ceder, *Nat. Chem.* **2016**, *8*, 692; b) G. Assat, J. Tarascon, *Nat. Energy* **2018**, *3*, 373.
- [6] a) B. Li, R. Shao, H. Yan, L. An, B. Zhang, H. Wei, J. Ma, D. Xia, X. Han, *Adv. Funct. Mater.* **2016**, *26*, 1330; b) M. Saubanère, E. McCalla, J. M. Tarascon, M. L. Doublet, *Energy Environ. Sci.* **2016**, *9*, 984; c) K. Zhang, B. Li, Y. Zuo, J. Song, H. Shang, F. Ning, D. Xia, *Electrochem. Energy Rev.* **2019**, *2*, 606.
- [7] a) J. R. Croy, K. G. Gallagher, M. Balasubramanian, Z. Chen, Y. Ren, D. Kim, S. Kang, D. W. Dees, M. M. Thackeray, *J. Phys. Chem. C* **2013**, *117*, 6525; b) G. Assat, D. Foix, C. Delacourt, A. Iadecola, R. Dedryvère, J.-M. Tarascon, *Nat. Commun.* **2017**, *8*, 2219; c) F. Dogan, B. R. Long, J. R. Croy, K. G. Gallagher, H. Iddir, J. T. Russell, M. Balasubramanian, B. Key, *J. Am. Chem. Soc.* **2015**, *137*, 2328; d) W. E. Gent, K. Lim, Y. Liang, Q. Li, T. Barnes, S. Ahn, K. H. Stone, M. McIntire, J. Hong, J. H. Song, Y. Li, A. Mehta, S. Ermon, T. Tyliczszak, D. Kilcoyne, D. Vine, J. Park, S. Doo, M. F. Toney, W. Yang, D. Prendergast, W. C. Chueh, *Nat. Commun.* **2017**, *8*, 2091.
- [8] a) J. An, L. Shi, G. Chen, M. Li, H. Liu, S. Yuan, S. Chen, D. Zhang, *J. Mater. Chem. A* **2017**, *5*, 19738; b) G. Chen, J. An, Y. Meng, C. Yuan, B. Matthews, F. Dou, L. Shi, Y. Zhou, P. Song, G. Wu, D. Zhang, *Nano Energy* **2019**, *57*, 157; c) X. Zhang, J. Shi, J. Liang, Y. Yin, J. Zhang, X. Yu, Y. Guo, *Adv. Mater.* **2018**, *30*, 1801751.
- [9] S. Shen, Y. Hong, F. Zhu, Z. Cao, Y. Li, F. Ke, J. Fan, L. Zhou, L. Wu, P. Dai, M. Cai, L. Huang, Z. Zhou, J. Li, Q. Wu, S. Sun, *ACS Appl. Mater. Interfaces* **2018**, *10*, 12666.
- [10] G. Assat, C. Delacourt, D. A. D. Corte, J. Tarascon, *J. Electrochem. Soc.* **2016**, *163*, A2965.
- [11] a) J. R. Croy, M. Balasubramanian, K. G. Gallagher, A. K. Burrell, *Acc. Chem. Res.* **2015**, *48*, 2813; b) L. Zhang, H. Noguchi, *J. Electrochem. Soc.* **2003**, *150*, A601; c) B. Li, D. Xia, *Adv. Mater.* **2017**, *29*, 1701054; d) W. Li, B. Song, A. Manthiram, *Chem. Soc. Rev.* **2017**, *46*, 3006; e) S. Han, Y. Xia, Z. Wei, B. Qiu, L. Pan, Q. Gu, Z. Liu, Z. Guo, *J. Mater. Chem. A* **2015**, *3*, 11930.
- [12] a) F. Yu, L. Que, Z. Wang, Y. Xue, Y. Zhang, B. Liu, D. Gu, *J. Mater. Chem. A* **2017**, *5*, 9365; b) M. Wang, F. Yu, G. Sun, D. Gu, Z. Wang, *ACS Appl. Energy Mater.* **2018**, *1*, 4158.
- [13] a) K. Luo, M. R. Roberts, R. Hao, N. Guerrini, D. M. Pickup, Y. Liu, K. Edström, J. Guo, A. V. Chadwick, L. C. Duda, P. G. Bruce, *Nat. Chem.* **2016**, *8*, 684; b) G. Assat, J. Tarascon, *Nat. Energy* **2018**, *3*, 373.
- [14] L. de Biasi, B. Schwarz, T. Brezesinski, P. Hartmann, J. Janek, H. Ehrenberg, *Adv. Mater.* **2019**, *31*, 1900985.
- [15] a) K. Luo, M. R. Roberts, N. Guerrini, N. Tapia-Ruiz, R. Hao, F. Massel, D. M. Pickup, S. Ramos, Y. Liu, J. Guo, A. V. Chadwick, L. C. Duda, P. G. Bruce, *J. Am. Chem. Soc.* **2016**, *138*, 11211; b) J. Xu, M. Sun, R. Qiao, S. E. Renfrew, L. Ma, T. Wu, S. Hwang, D. Nordlund, D. Su, K. Amine, J. Lu, B. D. McCloskey, W. Yang, W. Tong, *Nat. Commun.* **2018**, *9*, 947.
- [16] R. A. House, U. Maitra, M. A. Pérez-Osorio, J. G. Lozano, L. Jin, J. W. Somerville, L. C. Duda, A. Nag, A. Walters, K. Zhou, M. R. Roberts, P. G. Bruce, **2020**, 577, 502.
- [17] a) W. He, J. Liu, W. Sun, W. Yan, L. Zhou, C. Wu, J. Wang, X. Yu, H. Zhao, T. Zhang, Z. Zou, *ACS Appl. Mater. Interfaces* **2018**, *10*, 23018; b) J. R. Croy, K. G. Gallagher, M. Balasubramanian, B. R. Long, M. M. Thackeray, *J. Electrochem. Soc.* **2014**, *161*, A318; c) B. Wu, X. Yang, X. Jiang, Y. Zhang, H. Shu, P. Gao, L. Liu, X. Wang, *Adv. Funct. Mater.* **2018**, *28*, 1803392.
- [18] Z. H. Lu, L. Y. Beaulieu, R. A. Donabarger, C. L. Thomas, J. R. Dahn, *J. Electrochem. Soc.* **2002**, *149*, A778.
- [19] X. Li, Y. Qiao, S. Guo, Z. Xu, H. Zhu, X. Zhang, Y. Yuan, P. He, M. Ishida, H. Zhou, *Adv. Mater.* **2018**, *30*, 1705197.
- [20] J. Shi, J. Zhang, M. He, X. Zhang, Y. Yin, H. Li, Y. Guo, L. Gu, L. Wan, *ACS Appl. Mater. Interfaces* **2016**, *8*, 20138.
- [21] a) G. Sun, X. Yin, W. Yang, A. Song, C. Jia, W. Yang, Q. Du, Z. Ma, G. Shao, *Phys. Chem. Chem. Phys.* **2017**, *19*, 29886; b) D. Luo, S. Fang, L. Yang, S. Hirano, *ChemSusChem* **2017**, *10*, 4845.
- [22] P. Lanz, C. Villevieille, P. Novák, *Electrochim. Acta* **2014**, *130*, 206.
- [23] Y. Zheng, L. Chen, Y. Su, J. Tan, L. Bao, Y. Lu, J. Wang, R. Chen, S. Chen, F. Wu, *J. Mater. Chem. A* **2017**, *5*, 24292.
- [24] Y. Wang, X. Bie, K. Nikolowski, H. Ehrenberg, F. Du, M. Hinterstein, C. Wang, G. Chen, Y. Wei, *J. Phys. Chem. C* **2013**, *117*, 3279.
- [25] a) J. Zhang, F. Cheng, S. Chou, J. Wang, L. Gu, H. Wang, H. Yoshikawa, Y. Lu, J. Chen, *Adv. Mater.* **2019**, *31*, 1901808; b) G. Sun, F. Yu, L. Que, L. Deng, M. Wang, Y. Jiang, G. Shao, Z. Wang, *Nano Energy* **2019**, *66*, 104102.
- [26] R. Shunmugasundaram, R. S. Arumugam, J. R. Dahn, *Chem. Mater.* **2015**, *27*, 757.
- [27] B. Li, H. Yan, J. Ma, P. Yu, D. Xia, W. Huang, W. Chu, Z. Wu, *Adv. Funct. Mater.* **2014**, *24*, 5112.
- [28] S. J. Clark, M. D. Segall, C. J. Pickard, P. J. Hasnip, M. J. Probert, K. Refson, M. C. Payne, *Z. Kristallogr.* **2005**, *220*, 567.